# Protection of Sensitive Loads Using Sliding Mode Controlled Three-Phase DVR With Adaptive Notch Filter

Samet Biricik, *Member, IEEE*, Hasan Komurcugil, *Senior Member, IEEE*, Nguyen Duc Tuyen, and Malabika Basu, *Member, IEEE*

***Abstract*—This study introduces a sliding mode control (SMC) strategy for three-phase dynamic voltage restorers (DVRs) with 12-switch voltage source inverter (VSI). The compensating voltage references needed in the SMC strategy are generated by an adaptive notch filter (ANF) which exhibits excellent performance under grid voltage anomalies such as voltage sags, swells, unbalanced and distorted grid voltage conditions. The consequence of using ANF eliminates the use of phase lock loop (PLL) or frequency lock loop (FLL) and low pass filter (LPF) which makes it distinguishable from the existing reference signal generation solutions. In addition, the use of SMC strategy with its attractive properties makes the control implementation simple. Theoretical results are supported by simulation results as well as real-time laboratory results over a range of grid voltage anomalies. These results show that the proposed control strategy not only offers an excellent dynamic response independent from the parameter variations and disturbances, but also compensates the voltage sags, swells and harmonics on the load terminals under the defined limits of the IEEE-519 standard.**

***Index Terms*—Adaptive notch filter, dynamic voltage restorer, sliding mode controller, voltage sag, voltage swell.**

## I. Introduction

THE commercial and industrial consumers of electrical power penetrated into the distribution system are increasingly demanding a netter power quality. The voltage distortions and fluctuations existing in the distribution system may adversely affect the sensitive loads like computing equipment, communication system, manufacturing process and adjustable speed drives. The voltage sag and swell problems arise by short-circuit faults in the system. In the case of the voltage sags, operation of the sensitive loads employed in the industry are highly affected which results in significant costs because of the production loss. In the literature, voltage sag and swell problems are described as a abrupt reduction or rise of the voltages varying from 10% to 90 % during sag and 110% to 180% during swell of its nominal value [1]. Beside these, because of the non-linear loads such as motor drives or power electronics devices, the load currents may contain current harmonic components. These currents in turn interact with the distribution line impedances and then distort the voltages at the load terminals.

In order to cope with these problems, dynamic voltage restorers (DVR) are widely used in the industry [2], [3]. A properly designed DVR not only solves the voltage related power quality problems, but also eliminates the source harmonic voltages on the load terminals [4]. Therefore, the main objective of a DVR is to inject a voltage in series with the grid voltage to keep the load voltage at required level for all times. In order to accomplish this objective, the DVR should be controlled by an appropriate control strategy capable of offering a fast dynamic response, high robustness to parameter variations, sinusoidal load voltage with low total harmonic distortion (THD) and small steady-state errors. In addition, its performance under distorted grid voltage conditions should be quite good so as to maintain the load voltage at required level.

Some of the control strategies are developed to compensate the voltage sags only [1], [5]-[7]. On the other hand, the control strategies proposed in [8]-[10] are able to compensate the voltage sags and voltage swells as well as the harmonics that arise during distorted grid. In most of the existing control methods devised for the DVRs, the synchronously rotating *dq* reference frame algorithm has been widely used to detect the voltage differences and to access the *dq* components of the voltages. However, the authors in [10] reported that the *dq* algorithm does not offer the possibility of detecting different frequency components. Also, it is unable to satisfy the required control objective during waveform distortions and unbalanced voltage sag conditions. Although the idea of adaptive notch filter (ANF) has already been employed in the control of active power filter in [11] and [12] with the aim of filtering the current harmonics, its performance in the control of DVR has not been yet studied. The ANF method with its excellent ability in extracting positive-sequence components from non-ideal signal was applied in both 3P3W system [11] and 3P4W system [12] as alternatives for conventional *dq*-filter. Those

Manuscript received August 4, 2017; revised January 18, 2018 and June 30, 2018; accepted August 30, 2018.

S. Biricik is with the Department of Electrical and Electronic Engineering, European University of Lefke, North Cyprus, Mersin 10, Turkey and with the School of Electrical and Electronic Engineering, Dublin Institute of Technology, Dublin, Ireland (e-mail: sbiricik@eul.edu.tr)

H. Komurcugil is with the Computer Engineering Department, Eastern Mediterranean University, Famagusta, North Cyprus, Mersin 10, Turkey (e-mail: hasan.komurcugil@emu.edu.tr). (corresponding author)

N. D. Tuyen is with the Shibaura Institute of Technology, Tokyo, Japan and also Hanoi University of Science and Technology (e-mail: m609504@shibaura-it.ac.jp)

M. Basu is with the School of Electrical and Electronic Engineering, Dublin Institute of Technology, Dublin, Ireland (e-mail: mbasu@ieee.org)

This article has been accepted for publication in a future issue of this journal, but has not been fully edited. Content may change prior to final publication. Citation information: DOI 10.1109/TIE.2018.2868303, IEEE Transactions on Industrial Electronics



studies also show that the ANF can be implemented in either αβ0- or *abc*-coordinate system. Owing to the fast response and robust dynamic performance, the ANF method can be utilized in some applications with high disturbances and signal pollution which eliminates the requirement of any high-pass or low-pass filtering as otherwise required by the conventional methods.

It is well known that the control strategy is as important as the inverter topology that affects the cost, steady-state and dynamic performances of the device. The sliding mode control (SMC) technique has received considerable attention in recent years due to its important advantages such as the strong robustness against parameter variations and disturbances, simplicity in implementation, fast dynamic response and guaranteed stability. The SMC technique with these advantages is successfully applied to the control of UPS inverters [13], [14], DC-DC buck converters [15], [16] and three-phase DVRs with transformer [17], and without transformer [18]. In all of these works, it is mentioned that the value of sliding constant (referred to as λ) determines the speed of dynamic response and existence region size of the sliding mode. While small valued sliding constant causes slow dynamic response, large valued sliding constant may lead to undesirable overshoots. The rotating sliding-line-based SMC with a time-varying sliding constant improves the dynamic response without paying attention to the existence region of the sliding mode [14]. In all of the existing SMC strategies, the selection of sliding constant is based on trial and error method without paying attention to the existence region. Recently, the authors in [19] established the relationship between the dynamic response and existence region of the sliding mode for a single-phase DVR.

In this paper, a SMC based control strategy in which the references of the compensation voltages are determined by the ANF is proposed for a three-phase DVR employing a 12-switch voltage source inverter (VSI). The proposed control strategy offers fast dynamic response, on-line estimation of the voltage anomalies on the grid voltages, strong robustness to voltage sags and swells and simplicity in implementation. In 12-switch DVR topology, instead of using a three-phase transformer, three single-phase transformers are used with the aim of reducing zero-sequence components. Moreover, this combination increases the flexibility and reliability of the system.

The organization of this paper is as follows. The studied DVR topology is introduced in Section II. The sliding mode controller with determination of its existence regions and adaptive notch filter are given in Section III. Finally, the simulations and experimental results are included in Sections IV and V.

## II. DVR WITH TWELVE SWITCH VSI

The circuit of the studied DVR is a three-phase 12-switch VSI with an energy storage battery as shown in Fig. 1. The energy storage is required to provide real power to the load during voltage injection to grid. The lead-acid batteries are good storage devices which can be used in DVR applications [21]-[23]. One of the main advantages of using a common battery source at the dc-link is that the dc-link voltage regulation with additional control algorithm is not required.

The common inverter topologies of three-phase DVR can be classified as: 6-switch three-phase inverter, 6-switch three-phase inverter with split-capacitor and 12-switch three-phase inverter. Although the 6-switch three-phase DVR has the simplest inverter topology with the minimum switches, this topology is unable to operate under unbalanced sag and swell voltage condition. The 6-switch three-phase inverter with split-capacitor topology requires additional control loop to balance the capacitor voltages. Moreover, compensation duration voltage compensation percentages are limited. Therefore, 12-switch three-phase inverter topology is the best candidate for compensating voltage swells and sags under unbalanced conditions. A detailed comparison between three-phase DVR topologies is presented in [24]. In the 12-switch DVR topology, the output of each 4-switch inverter is connected to the point of common coupling (PCC) through a low frequency single-phase transformer which achieves the galvanic isolation. The primary side of each transformer is connected between the utility and load line in series on each phase. In the conventional three-phase DVRs employing 6-switch VSI, the secondary side of the transformer is required to be connected to the VSI as delta [20] or star [4], [8]. However, there is no such delta or star connection in the 12-switch VSI. As can be seen in Fig. 1, the input and output terminals of the secondary side of the transformers are directly connected to the VSI terminals. Such converters are mostly preferred for the effective control on the zero-sequence components to cater for the unbalanced voltages or single-phase voltage sags. Therefore, this type of connection is very useful during the compensation of unbalanced utility voltages.

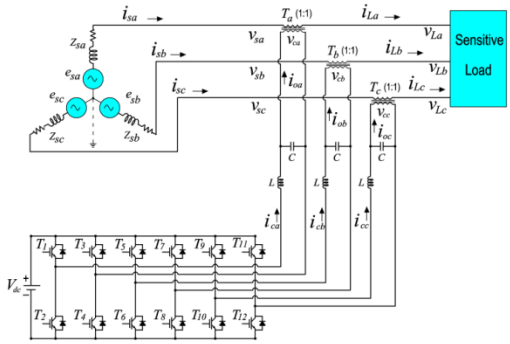


Fig. 1. Three-phase DVR with 12-switch VSI.

## III. PROPOSED CONTROL STRATEGY

In the literature, there are many control strategies devised for DVRs. Generally, these control strategies involve three main objectives such as the detection of voltage anomalies, generation of the reference signals needed for controlling the DVR, and suitable controller. In this study, the detection of voltage anomalies and generation of the reference signals are achieved by using ANF. The control of DVR is based on the SMC.

This article has been accepted for publication in a future issue of this journal, but has not been fully edited. Content may change prior to final publication. Citation information: DOI 10.1109/TIE.2018.2868303, IEEE Transactions on Industrial Electronics



### A. Sliding Mode Control

The switching devices shown in Fig. 1 should be operated such that the DVR injects the desired compensation voltage $(v_{cp})$ in series with the grid voltage $(v_{sp})$ through a series transformer $T_p(1:1)$ for each phase. The transformer is used to provide an electrical isolation between the VSI and grid. The grid impedance is represented by $Z_{sp}$. The differential equations regarding the operation of DVR can be written as

$$ki_{cp} = (u_p V_{dc} - v_{cp})/L \tag{1}$$

$$kv_{cp} = (i_{cp} - i_{sp})/C \tag{2}$$

where $k = d/dt$, $i_{cp}$ is the inductor current, $i_{sp}$ is the supply current, and $v_{cp}$ is the compensation voltage, $V_{dc}$ is the chargeable dc power supply, $L$ is the filter inductance, $C$ is the filter capacitance, $u_p$ is the control input, and $p = a,b,c$. The design of SMC is based on two important steps: determination of suitable sliding surface function and selection of suitable control law. The VSI topology used in this study is buck type (input dc voltage is always greater than the peak value of inverter's output voltage). Since the main goal here is to control inverter's output voltage, which is the compensation voltage in DVR, then using the compensation voltage error and its rate of change as the state variables for this inverter topology is the simplest and effective method in a SMC application [13], [14]. It is worth noting that using the inverter current error and compensation voltage error as the state variables would also yield satisfactory performance at the expense of increased controller complexity and cost due to the inverter current sensing requirement.

Now, let the compensation voltage error and its derivative be defined as

$$x_{1p} = v_{cp} - v_{cp}^* \quad , \quad x_{2p} = \dot{x}_{1p} = \dot{v}_{cp} - \dot{v}_{cp}^* \tag{3}$$

where $v_{cp}^*$ is the reference for the compensating voltage, $\dot{x}_{1p}$ is the derivative of $x_{1p}$, and $\dot{v}_{cp}$ is the derivative of $v_{cp}$. It is obvious from (3) that $v_{cp}^*$ is needed whose generation will be discussed in the next sub-section. Taking derivative of $x_{1p}$ and $x_{2p}$ yields

$$\dot{x}_{1p} = x_{2p} = \dot{v}_{cp} - \dot{v}_{cp}^* \quad , \quad \dot{x}_{2p} = \ddot{v}_{cp} - \ddot{v}_{cp}^* \tag{4}$$

Substituting (2) into $\dot{x}_{2p}$ yields

$$\dot{x}_{2p} = -k\dot{v}_{cp}^* + (ki_{cp} - ki_{sp})/C \tag{5}$$

Now, substituting (1) into (5), using $v_{cp} = x_{1p} + v_{cp}^*$ and $\omega_s^2 = 1/LC$ in the resulting equation gives

$$\dot{x}_{2p} = -\omega_s^2 x_{1p} + \omega_s^2 u_p V_{dc} - \omega_s^2 v_{cp}^* - k\dot{v}_{cp}^* - (ki_{sp})/C \tag{6}$$

Hence, the behaviour of the DVR in terms of $x_{1p}$ and $x_{2p}$ can be written as

$$\dot{x}_{1p} = x_{2p} \tag{7}$$

$$\dot{x}_{2p} = \omega_s^2 \left[ u_p V_{dc} - x_{1p} + D_p(t) V_{dc} \right] \tag{8}$$

where $D_p(t)$ is the disturbance described as

$$D_p(t) = (-Lki_{sp} - v_{cp}^* - LCk\dot{v}_{cp}^*)/V_{dc} \tag{9}$$

From (9), it can be seen that $D_p(t)$ is a time-varying function. The sliding surface function is defined as

$$S_p = \lambda x_{1p} + x_{2p} \tag{10}$$

where $\lambda$ is the positive sliding constant. The system enters into the sliding mode when $S_p = \dot{S}_p = 0$. In this case, the error variables are enforced to slide on the sliding surface towards the origin ( $x_{1p} = 0$ and $x_{2p} = 0$ ). The sliding mode is defined by the following equation

$$\dot{x}_{1p} = x_{2p} = -\lambda x_{1p} \tag{11}$$

The solution of (11) can easily be obtained as

$$x_{1p} = x_{1p}(0)e^{-\lambda t} \tag{12}$$

In order to keep the movement of the error variables on the sliding surface, the following condition must hold

$$S_p \dot{S}_p < 0 \tag{13}$$

Existence of the sliding mode is necessary due to the stability reason. Hence, if the control input $u_p$ is defined as

$$u_p = -sign(S_p) \tag{14}$$

then, the sliding mode exists if the following conditions are satisfied.

Condition I: When $S_p < 0 \Rightarrow u_p = 1$;

$$\dot{S}_p = -\omega_s^2 x_{1p} + \lambda x_{2p} + d_{1p}(t) > 0 \tag{15}$$

Condition II: When $S_p > 0 \Rightarrow u_p = -1$ ;

$$\dot{S}_p = -\omega_s^2 x_{1p} + \lambda x_{2p} + d_{2p}(t) < 0 \tag{16}$$

Equations (15) and (16) represent two parallel lines which constitute the boundaries of the existence region in the $(x_{1p}, x_{2p})$ plane. In (15) and (16), $d_{1p}(t)$ and $d_{2p}(t)$ are defined as

$$d_{1p}(t) = \omega_s^2 V_{dc} + D_p(t) \tag{17}$$

$$d_{2p}(t) = -\omega_s^2 V_{dc} + D_p(t) \tag{18}$$

It is apparent from (12) that λ controls the rate at which the compensation voltage error decays to zero. According to (15) and (16), λ also determines the borders of the existence region (not shown due to limited space). This fact was already mentioned by the authors in [19]. It is pointed out that while large λ would speed up the dynamic response, it causes a reduction in the existence region size which endangers the stability of the sliding mode. On the other hand, small λ not only slows down the dynamic response, but also reduces the size of existence region. Hence, the value of λ plays an important role in determining the desired dynamic response speed and sufficiently large existence region which

This article has been accepted for publication in a future issue of this journal, but has not been fully edited. Content may change prior to final publication. Citation information: DOI 10.1109/TIE.2018.2868303, IEEE Transactions on Industrial Electronics



ensures the stability. In most of the SMC studies published so far, the heuristic method is used to determine the optimum value of $\lambda$. Recently, the authors in [19] proposed an analytical method to find the optimum value of $\lambda$ which maximizes the existence region and improves the dynamic response of the compensation voltage error. It is shown that the optimum value of $\lambda$ depends on the output $LC$ filter. In this study, the selection of $\lambda$ was based on the method introduced in [19].

### B. Analysis of Chattering

The main drawback of SMC approach is chattering which appears as very high frequency oscillations caused by the ideal discontinuous control in (14). In order to suppress the chattering and avoid high switching frequency, (14) is modified with the hysteresis modulation using a hysteresis band as follows

$$u_p = \begin{cases} 1 & \text{when} \quad S_p < -h \\ -1 & \text{when} \quad S_p > +h \end{cases} \tag{19}$$

where $h$ denotes the hysteresis band. Evolution of $S_p$ is shown in Fig. 2.

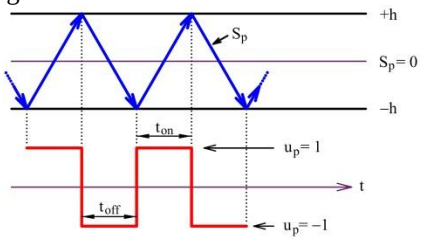


Fig. 2. Evolution of $S_p$.

Clearly, the sliding surface function moves between the upper and lower hysteresis bands. In the sliding mode, assuming that $x_{1p} \cong x_{2p} \cong 0$, then the derivative of (10) can be written as

$$\dot{S}_p \cong \omega_s^2 V_{dc}(u_p + D_p(t)) \tag{20}$$

where

$$D_p(t) = -\frac{V_{cp}}{V_{dc}}(1-\omega^2 LC)\sin(\omega_0 t) - \frac{\omega L I_{Lp}}{V_{dc}}\cos(\omega_0 t - \psi) \tag{21}$$

In (21), the load current and compensation voltage reference are assumed to be $i_{Lp} = I_{Lp}\sin(\omega_0 t - \psi)$ and $v_{cp}^* = V_{cp}\sin(\omega_0 t)$. The disturbance term $D_p(t)$ can be written in terms of single cosine term as follows

$$D_p(t) = D_m \cos(\omega_0 t - \phi) \tag{22}$$

where

$$\begin{aligned} D_m &= \sqrt{D_1^2 + D_2^2 + 2D_1 D_2 \sin\psi} \\ D_1 &= \frac{V_{cp}}{V_{dc}}(1-\omega^2 LC)\ ,\ D_2 = \frac{\omega L I_{Lp}}{V_{dc}} \\ \phi &= \tan^{-1}\left((D_1 + D_2\sin\psi)/D_2\right) \end{aligned} \tag{23}$$

Using the system parameters in Appendix, $\phi$ is computed to be $86.56^\circ$ which can be approximated as $\phi \cong 90^\circ$. Hence, the disturbance can be written as

$$D_p(t) = D_m \sin(\omega_0 t) \tag{24}$$

From Fig. 2, one can easily obtain

$$t_{on} = \frac{2h}{\dot{S}_p\big|_{u_p=1}} = \frac{2h}{\omega_s^2 V_{dc}(1 + D_m \sin\omega_0 t)} \tag{25}$$

$$t_{off} = \frac{-2h}{\dot{S}_p\big|_{u_p=-1}} = \frac{2h}{\omega_s^2 V_{dc}(1 - D_m \sin\omega_0 t)} \tag{26}$$

Now, the switching frequency can be easily written as

$$f_{sw} = \frac{\omega_s^2 V_{dc}}{4h}(1 - D_m^2 \sin^2(\omega_0 t)) \tag{27}$$

It can be seen that $f_{sw} = \infty$ under ideal discontinuous control $(h = 0)$. Hence, the larger the value of $h$, the smaller the amount of chattering in the system states.

### C. Detection of Voltage Anomalies and Generation of Compensating Voltage References Using ANF

As mentioned in the previous sub-section, the generation of compensating voltage references $(v_{cp}^*)$ is essential in the SMC. The SMC is solely designed to regulate and balance the load voltage amplitudes at the fundamental frequency. The undistorted and balanced three-phase voltages on the load terminals are given by

$$\left.\begin{aligned} v_{La}(t) &= V_{La}\sin(\omega_0 t + \phi) = 230\sqrt{2}\sin(2\pi 50 t) \\ v_{Lb}(t) &= V_{Lb}\sin(\omega_0 t + \phi) = 230\sqrt{2}\sin(2\pi 50 t - \frac{2\pi}{3}) \\ v_{Lc}(t) &= V_{Lc}\sin(\omega_0 t + \phi) = 230\sqrt{2}\sin(2\pi 50 t + \frac{2\pi}{3}) \end{aligned}\right\} \tag{28}$$

The control of load voltage amplitudes $(V_{Lp})$ is relatively easy. However, most of the control strategies devised for DVRs may fail under distorted utility voltage conditions. Therefore, an effective method is essential to detect the voltage harmonics. The ANF algorithm is a good candidate to extract the undistorted reference voltages and grid frequency information from the distorted grid [25], [26]. Before adopting the ANF algorithm to the DVR system, we assume that the three-phase grid voltages are distorted by the voltage harmonics and are unbalanced as follows

$$\left.\begin{aligned} v_{sa}(t) &= 240\sqrt{2}\sin(\omega_0 t) + 30\sin(5\omega_0 t) \\ &\quad + 20\sin(7\omega_0 t) + 7\sin(11\omega_0 t) \\ v_{sb}(t) &= 226\sqrt{2}\sin(\omega_0 t - \frac{2\pi}{3}) + 35\sin(5\omega_0 t - \frac{2\pi}{3}) \\ &\quad + 9\sin(7\omega_0 t - \frac{2\pi}{3}) + 10\sin(11\omega_0 t - \frac{2\pi}{3}) \\ v_{sc}(t) &= 247\sqrt{2}\sin(\omega_0 t + \frac{2\pi}{3}) + 19\sin(5\omega_0 t + \frac{2\pi}{3}) \\ &\quad + 15\sin(7\omega_0 t + \frac{2\pi}{3}) + 13\sin(11\omega_0 t + \frac{2\pi}{3}) \end{aligned}\right\} \tag{29}$$

The characteristic time domain model of transfer functions of the ANF is represented as follows

This article has been accepted for publication in a future issue of this journal, but has not been fully edited. Content may change prior to final publication. Citation information: DOI 10.1109/TIE.2018.2868303, IEEE Transactions on Industrial Electronics



$$\left.\begin{aligned}\ddot{v}_{sp}(t) &= \theta\left[\zeta\, e_{sp}(t) - \theta\, v_{sp}(t)\right] \\ \dot{v}_{sp}(t) &= v_{sp}(t) - e_{sp}(t) \\ \dot{\theta} &= -\gamma\, v_{sp}(t)\theta\, e_{sp}(t)\end{aligned}\right\} \tag{30}$$

where $v_{sp}(t)$ is the measured three-phase grid voltages, $\theta$ is the estimated frequency for nominal system frequency ($\omega_0$), $\zeta$ and $\gamma$ are adjustable real positive parameters that respectively determine the estimation accuracy and the capability of the algorithm in tracking the grid voltage characteristics variations. The error signal for each phase is defined as $e_{sp}(t) = v_{sp}(t) - [V_{Lp}\sin(\omega_0 t + \varphi)]$ and the derivative of the state variable $v_{sp}(t)$ is the fundamental component of the input voltage. For the sake of simplicity, the subscript "*sp*" is dropped from $e_{sp}(t)$ and $\dot{v}_{sp}(t)$. Hence, the transfer function from $E(s)$ to $\dot{V}(s)$ is given by

$$G_e(s) = \frac{\dot{V}(s)}{E(s)} = \frac{\zeta\,\theta\, s}{s^2 + \theta^2} \tag{31}$$

where $E(s)$ and $\dot{V}(s)$ denote the Laplace transforms of the error signal $e_{sp}(t)$ and derivative of grid voltage $\dot{v}_{sp}(t)$, respectively. Rewriting $G_e(s)$ in the frequency domain yields

$$G_e(j\omega) = j\,\frac{\zeta\omega\theta}{\theta^2 - \omega^2} = \frac{\zeta\omega\theta}{\theta^2 - \omega^2}\angle\pi/2 \tag{32}$$

where $\omega$ is the angular frequency of the source voltage and $\zeta$ is the damping factor of the ANF algorithm. From (32), when $\omega = \theta$, $\left\|G_e(j\omega)\right\| = \infty$ and the error vanishes according to (31). In other words, the fundamental component can thoroughly pass through the ANF. In order to tune $\zeta$, the system is considered at the steady state as $\theta = \omega_0$. Assuming that $\omega_c$ is the crossover frequency of the open loop system (the transfer path from $E(s)$ to $\dot{V}(s)$), the gain of $G_e(j\omega)$ at $\omega_c$ must be unity:

$$\left\|G_e(j\omega_c)\right\| = \zeta\,\frac{\omega_c\omega_0}{\omega_0^2 - \omega_c^2} = 1 \tag{33}$$

Solving for $\zeta$ gives

$$\zeta = \frac{\omega_0}{\omega_c} - \frac{\omega_c}{\omega_0} \tag{34}$$

Fig. 3 shows the bandpass effect of the ANF. It is evident that only the signal whose frequency ranges from $\omega_c$ to $\omega_c^2/\omega_c$ is passed through the filter. The rate of convergence of ANF is proportional to the width of the band:

$$T_c \approx \frac{2\pi}{(\omega_0^2/\omega_c) - \omega_c} = \frac{2\pi}{\zeta\,\omega_0} \tag{35}$$

It is obvious from (35) that the wider the band width the faster the rate of convergence can be obtained.

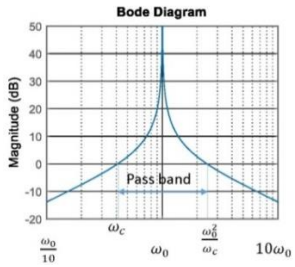


Fig. 3. Bandpass effect of ANF.

In such a case, the output signal also contains more harmonics whose frequency is close to the fundamental $\omega_0$. On the other hand, narrower band width takes longer time to vanish the error signal. However, in this case, the harmonics of output signal are eliminated mostly. Accordingly, the reasonable value for $\zeta$ should vary between 0.2 to 2 depending on the frequency and the desired quality of the output signal.

Also, there is a need to tune $\gamma$. For this issue, the dynamic model of $\theta$ is

$$\dot{\theta} = -\gamma v_{sp}(t) e_{sp}(t)\theta = \frac{\gamma}{\zeta} v_{sp}(t)\left[\ddot{v}_{sp}(t) + \theta^2 v_{sp}(t)\right] \tag{36}$$

In the steady state, since $\dot{\theta} = 0$, $\ddot{v}_{sp}(t) \to \ddot{\bar{v}}_{sp}(t)$ and $v_{sp}(t) \to \bar{v}_{sp}(t)$, then we have

$$\left.\begin{aligned}\theta &= \omega_0 \\ \ddot{\bar{v}}_{sp}(t) &= -\omega_0^2 \bar{v}_{sp}(t)\end{aligned}\right\} \tag{37}$$

Now, let $\hat{\theta}$ be the small signal component of $\theta$. $\hat{\theta}$ denotes the small variations of $\theta$ around $\omega_0$ such that

$$\theta = \omega_0 + \hat{\theta} \tag{38}$$

For the initial condition of the integrator, $\omega_0$ is set to $100\pi$. From (36) and (37), the small signal model can be written as

$$\dot{\hat{\theta}} = -\frac{\gamma}{\zeta}\bar{v}_{sp}^2(t)\left(\hat{\theta}^2 + 2\hat{\theta}\omega_0\right) \tag{39}$$

Since $\hat{\theta}$ is a small signal, $\hat{\theta}^2$ can be neglected. Therefore, the model in (39) reduces to

$$\dot{\hat{\theta}} = -\frac{2\gamma\omega_0\hat{\theta}}{\zeta}\bar{v}_{sp}^2(t) \tag{40}$$

Once the system (40) is stable, its eigenvalue ($\sigma$) must be placed at the left half plane of the Re-Im surface, where

$$\sigma = -\frac{2\gamma\omega_0}{\zeta}\bar{v}_{sp}^2(t) \tag{41}$$

From another aspect, if the fundamental of $v_{sp}(t)$ is

$$v_{sp}(t) = V_{sp}\sin(\omega_0 t) \tag{42}$$

then, the state variable $\bar{v}_{sp}(t)$ is given by

$$\bar{v}_{sp}(t) = \frac{V_{sp}}{\omega_0}\cos(\omega_0 t) \tag{43}$$

Substituting (43) into (41) yields

$$\sigma = -\frac{2\gamma\omega_0}{\zeta}\left(\frac{V_{sp}}{\omega_0}\right)^2\cos^2(\omega_0 t) \tag{44}$$

This article has been accepted for publication in a future issue of this journal, but has not been fully edited. Content may change prior to final publication. Citation information: DOI 10.1109/TIE.2018.2868303, IEEE Transactions on Industrial Electronics



where $\omega_0$ is the angular (center) frequency of the source voltage. By assigning,

$$\gamma = \frac{\zeta}{2}\left(\frac{\omega_0}{V_{sp}}\right)^2 \tag{45}$$

the eigenvalue $\sigma$ is placed around $-\omega_0$. As a consequence, the system is always stable with the rate of convergence proportional to $2\pi/\omega_0$. In addition, the stability of the proposed system (both ANF and SMC) is not degraded when the compensating voltage reference is generated inaccurately. In this case, as mentioned just after (35), the ANF cannot produce the desired compensating voltage reference immediately after the occurrence of the voltage sag (or swell). Eventually, the dynamic response of the controller becomes faster (or slower) depending on the value of $\zeta$. In order to investigate the performance of SMC, let the inaccurate compensating voltage reference be determined by

$$\hat{v}_{cp}^{*} = v_{cp}^{*} + \varepsilon \tag{46}$$

where $\varepsilon$ denotes the error involved in the compensating voltage reference. Substituting (46) into (3) and (9) yields

$$\hat{x}_{1p} = x_{1p} - \varepsilon \quad , \quad \hat{x}_{2p} = x_{2p} - \dot{\varepsilon} \tag{47}$$

$$\hat{D}_p(t) = D_p(t) - (\varepsilon + LCk\dot{\varepsilon})/V_{dc} \tag{48}$$

Now, substituting (47) and (48) into (15) and (16) gives

$$l_{1p} = -\omega_s^2 x_{1p} + \lambda x_{2p} + d_{1p}(t) + \omega_s^2\varepsilon - \lambda\dot{\varepsilon} - \frac{1}{V_{dc}}(\varepsilon + LCk\dot{\varepsilon}) > 0 \tag{49}$$

$$l_{2p} = -\omega_s^2 x_{1p} + \lambda x_{2p} + d_{2p}(t) + \omega_s^2\varepsilon - \lambda\dot{\varepsilon} - \frac{1}{V_{dc}}(\varepsilon + LCk\dot{\varepsilon}) < 0 \tag{50}$$

$l_{1p}$ and $l_{2p}$ represent two parallel lines which determine the boundaries of the stability region in the reaching mode in $x_{1p} - x_{2p}$ plane (not shown due to limited space). Comparing, (15) and (16) with (49) and (50), one can see that the intersection points of (49) and (50) have additional terms due to $\varepsilon$. This means that the stability region still exists, but its borders are changed slightly. On the other hand, when the system enters into the sliding mode with $\hat{v}_{cp}^{*}$, (11) becomes $\dot{\hat{x}}_{1p} = -\lambda\hat{x}_{1p}$ whose solution $\hat{x}_{1p} = \hat{x}_{1p}(0)e^{-\lambda t}$ depends neither on the system parameters nor the disturbance. In this case, $\hat{x}_{1p}$ converges to zero (which means that $x_{1p} = \varepsilon$) without any stability problem. Figs. 6, 8, and 9 (see Sections IV and V) verify that the stability is not degraded when the ANF generates inaccurate compensating voltage reference during the occurrence of voltage sag. The block diagram of the proposed ANF is shown in Fig. 4. The consequence of using ANF eliminates the use of phase lock loop (PLL), frequency lock loop (FLL) and low pass filter (LPF) which makes it distinguishable from the existing reference signal generation methods such as second-order generalized integrator (SOGI) and self-tuning filter (STF) used in [17] and [19], respectively.

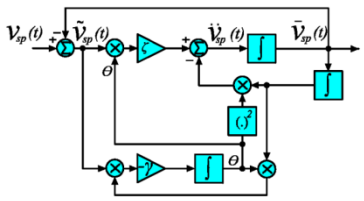


Fig. 4. Block diagram of the proposed ANF.

In order to determine the voltages which involve the anomalies, the source voltages generated with ANF algorithm are subtracted from the measured source voltages as follows

$$\tilde{v}_{sp}(t) = v_{sp}(t) - \bar{v}_{sp}(t) \tag{51}$$

The voltage difference for each phase can be determined by subtracting the reference load voltage waveform from the measured source voltage as follows

$$v_{dp}(t) = v_{sp}(t) - v_{Lp}^{*}(t) \tag{52}$$

The total compensating voltage reference is obtained by adding the voltage harmonic components obtained from (51) to the voltage difference obtained from (52) as follows

$$v_{cp}^{*}(t) = \tilde{v}_{sp}(t) + v_{dp}(t) \tag{53}$$

The total compensating voltage reference for each phase can be used as a reference input to the SMC which is discussed in the previous section.

## IV. Simulation Results

The performance of the proposed control strategy has been tested by simulations using MATLAB/Simulink. The block diagram of the closed-loop system is shown in Fig. 5. The system and control parameters used in the simulation and experimental studies are given in Appendix. Performance of the proposed control method with the control methods in [18] and [19] are compared under four different grid voltage conditions (case 1, case 2, case 3, and case 4). In case 1, it is assumed that a balanced voltage sag occurs (from 230V to 150V) in all phases of the grid voltage for 50ms. In case 2, it is assumed that an unbalanced voltage sag occurs in phases A and B of the grid for 50ms. In case 3, the voltage swell of 120% (from 230V to 276V) occurs in phases A and B of the grid for 50ms. Finally, in case 4, the grid voltage (all phases) is assumed to be highly distorted for 50ms. The simulation results regarding these conditions are shown in Fig. 6(a).

Fig. 6 shows the simulation results obtained from the methods in [18], [19] and proposed control method during the grid voltage conditions described above. While Figs. 6(b) and (e) belong to the method in [18], Figs. 6(c) and (f) belong to the method in [19]. The results obtained with the proposed method are shown in Figs. 6(d) and (g). The balanced voltage sag described in case 1 starts at t=0.05s and lasts until t=0.1s as shown in Fig. 6(a). Despite 65% voltage sag, the load voltages were compensated dynamically in all phases as can be seen in Figs. 6(e), (f) and (g). The unbalanced voltage sag described in case 2 starts at t=0.1s and lasts until t=0.15s as shown in Fig. 6(a). Note that the grid voltage at phase-C is not changed during this interval. Again, the load voltages for phases A and B were compensated successfully as shown in Figs. 6(e), (f) and (g). It is evident that the VSI does not produce any compensation voltage for phase-C as shown in Figs. 6(b), (c) and (d). The voltage swell condition described

This article has been accepted for publication in a future issue of this journal, but has not been fully edited. Content may change prior to final publication. Citation information: DOI 10.1109/TIE.2018.2868303, IEEE Transactions on Industrial Electronics



in case 3 starts at t=0.15s until t=0.2s as shown in Fig. 6(a). It can be seen from Figs. 6(b), (c) and (d) that the DVR injects the necessary compensation voltages to phases A and B to keep the load voltages at desired level. Performance of the proposed control strategy was also tested under distorted grid voltage condition described in case 4. As can be seen from Fig. 6(a), the three-phase grid voltages after t=0.2s are highly distorted. The THD of the grid voltages in each phase are computed as 14.06%, 14.75% and 12.61%. Despite the highly distorted grid voltages, the DVR injects the required compensating voltages to suppress the voltage harmonics before they reach to the load terminals. As a consequence of this harmonic suppression, the load voltages were maintained at desired level.

Comparing Figs. 6(b), (c), (e), and (f) with Figs. 6(d) and (g), the dynamic response of the proposed control method is seen to be much faster than that of proposed in [18] and [19] during case 1. Although the performances of these control methods are comparable in the other grid conditions, the proposed control with ANF yields simpler structure due to its advantage that does not require PLL.

Fig. 7 shows the sliding surface function and state trajectory in the phase plane (phase A only) under case 1. It can be seen from Fig. 7(a) that the sliding surface function is bounded by the hysteresis bands which are introduced to limit the chattering. In the start-up, both state variables ($x_{1a}$ and $x_{2a}$) are zero as shown in Fig 7(b). When the system starts, the trajectory moves away from the equilibrium point in the negative direction until it reaches to the sliding line ($S_a$=0) where the sliding mode operation is started. Thereafter, the trajectory moves along the sliding line by making zigzag motions until the equilibrium point is reached as shown in Fig. 7(c). It is worth noting that the effect of voltage sag condition is not shown in Fig. 7(c) due to the fast response of the controller.

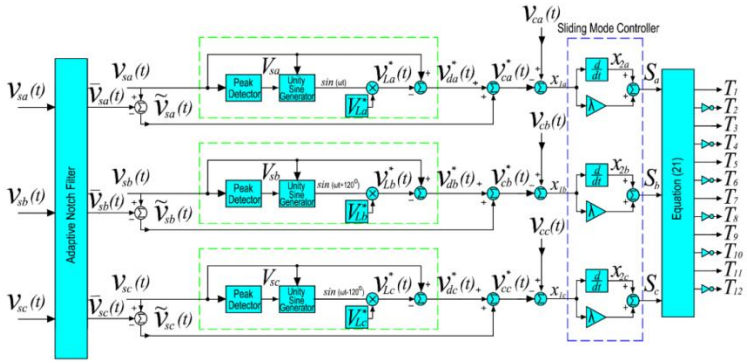


Fig. 5. Block diagram of the proposed control strategy.

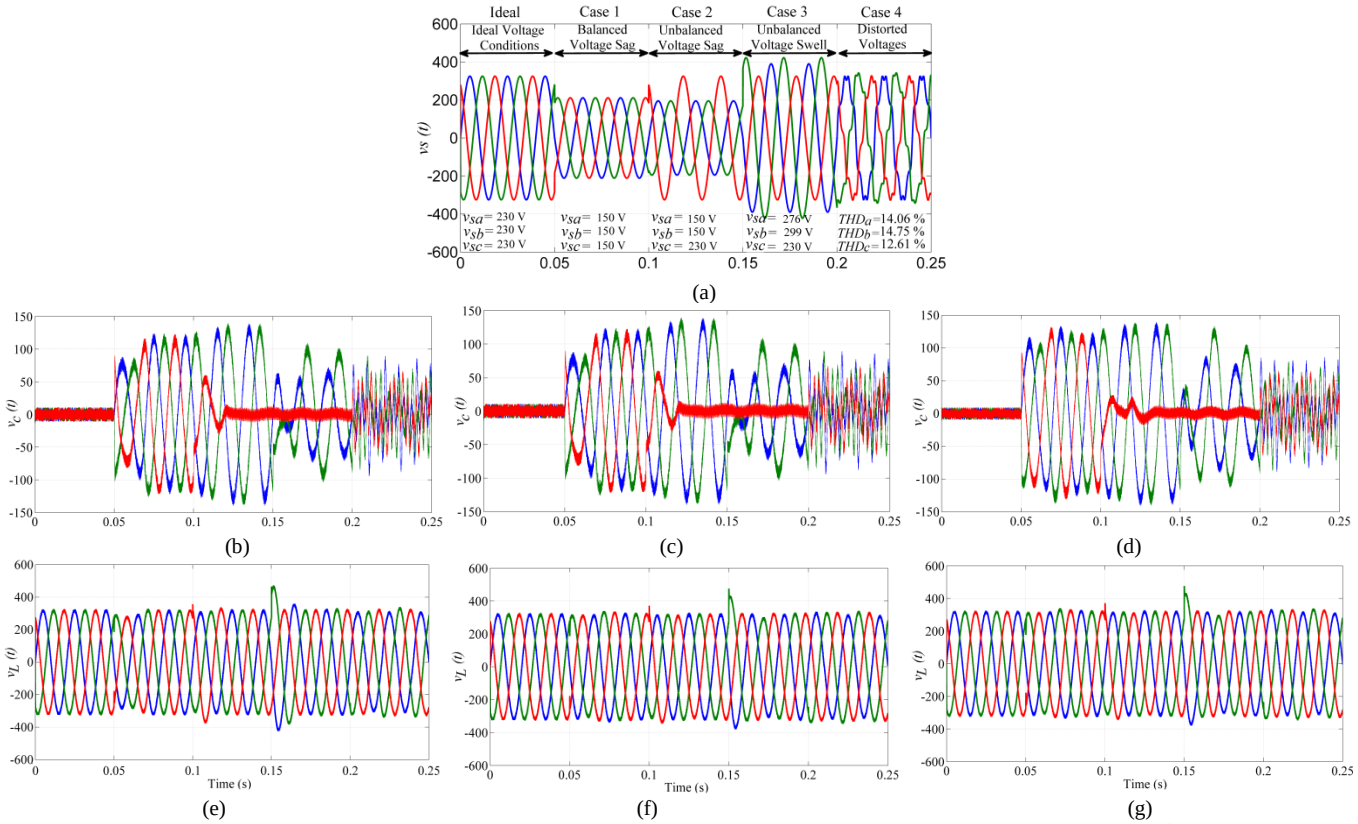


(a) (b) (c) (d) (e) (f) (g)

Fig. 6. Simulation results under (a) various grid voltage anomalies obtained with the methods presented in [18] (b) & (e), [19] (c) & (f) and proposed control method (d) & (g).

This article has been accepted for publication in a future issue of this journal, but has not been fully edited. Content may change prior to final publication. Citation information: DOI 10.1109/TIE.2018.2868303, IEEE Transactions on Industrial Electronics



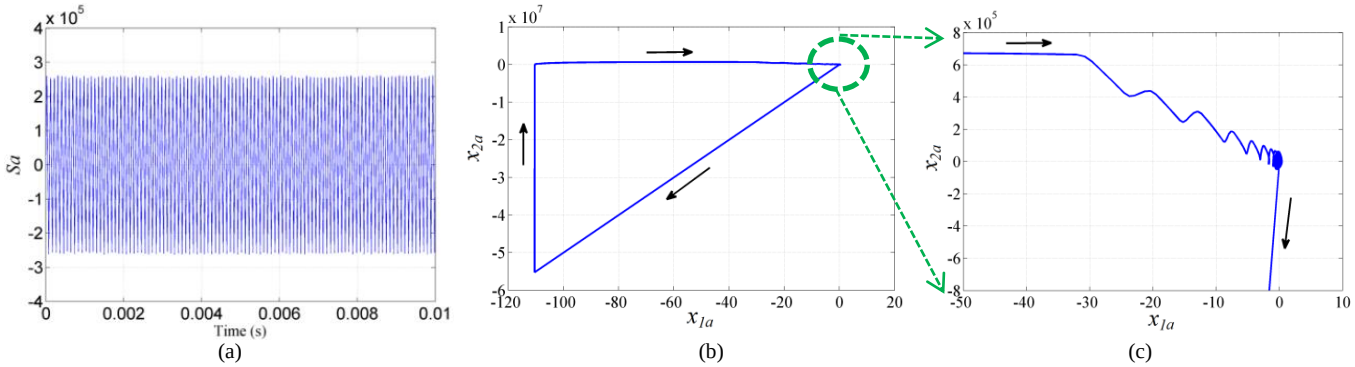


(a) (b) (c)

Fig. 7. (a) Sliding surface function, (b) State trajectory for start-up and case 1 in the phase-plane, (c) Magnified view of the trajectory in (b).

## V. Experimental Results

In order to observe the performance in a real time environment, the 12-switch DVR with the proposed control strategy has been modeled in Simulink using OPAL-RT real-time platform and associated tools. The system is then tested with hardware synchronization mode to obtain the real-time communications among the sensing and control signals. The OPAL-RT is a real-time simulation platform working under RT-LAB software environment. It has 16 analog inputs and outputs, 32 digital inputs and outputs.

Figs. 8 to 12 show the real-time results that correspond to the simulation results in Fig. 6. Fig. 8(a) shows the three-phase voltage sags (from 230V (rms) to 150 V (rms)) that occur on the grid voltage for case 1. When the voltage sags occur, the DVR injects the required compensation voltages to the PCC through the series transformers as shown in Fig. 8(b). As a result of this, the effects of voltage sags on the load terminals are strongly eliminated as displayed in Fig. 8(c). Fig. 9(a) shows the voltage sags (voltage is reduced from 230V to 150V) that occur at phase-A and phase-B for case 2. Fig. 9(b) shows that the DVR injects the compensation voltages for phase-A and phase-B so as to maintain the load voltages at desired level as shown in Fig. 9(c). This case shows that the proposed control strategy has strong ability to operate independently from the phases.

The voltage swells existing on phase-B and phase-C (for case 3) are shown in Fig. 10(a). Despite this swell condition, the DVR successfully injects the required voltages as shown in Fig. 10(b) and achieves the compensation of the load voltages as shown in Fig 10(c). It is worth to note that the DVR does not generate a compensation voltage for phase-A because there was no voltage swell for this phase.

Fig. 11(a) shows highly distorted and unbalanced grid voltages, for case 4, together with their measured THD values. The injected and load voltages are shown in Fig. 11(b) and Fig. 11(c), respectively. Despite the highly distorted grid voltage, the proposed control method reduces the load voltage THD to 2% (see Fig. 12), thereby satisfying the IEEE 519-1992 standards on the harmonic limits [27].

The harmonic spectrums of the grid and load voltages for case 4 are shown in Figs. 12(a) and (b), respectively. It is evident that 3rd, 5th and 7th harmonic components do not appear in the harmonic spectrum of the load voltage.

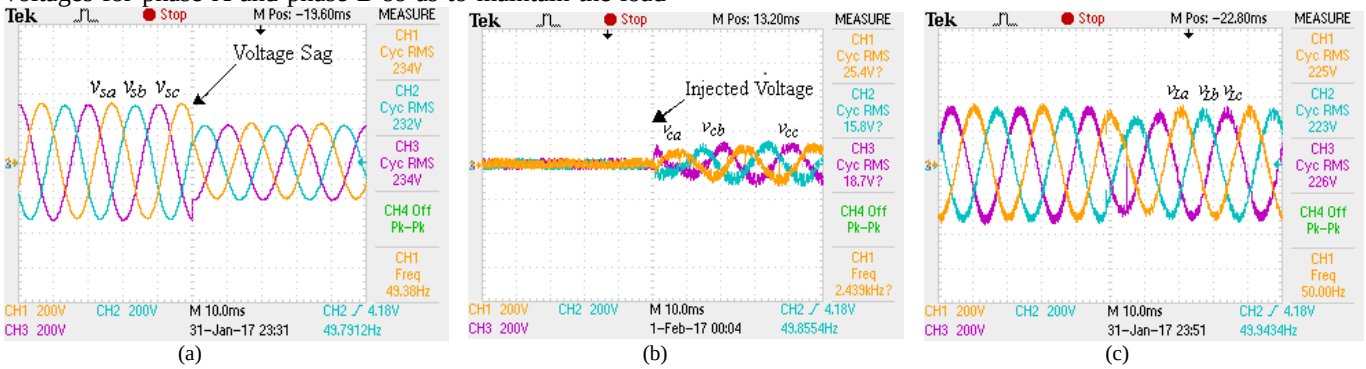


(a) (b) (c)

Fig. 8. Experimental results for case 1, (a) Grid voltages, (b) Injected voltages, (c) Load voltages.

This article has been accepted for publication in a future issue of this journal, but has not been fully edited. Content may change prior to final publication. Citation information: DOI 10.1109/TIE.2018.2868303, IEEE Transactions on Industrial Electronics



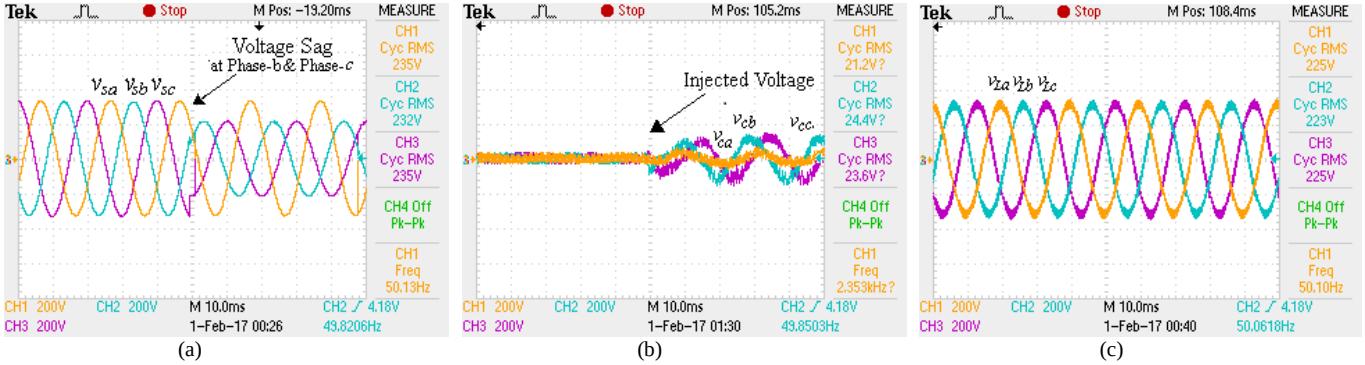


(a) (b) (c)

Fig. 9. Experimental results for case 2, (a) Grid voltages, (b) Injected voltages, (c) Load voltages.

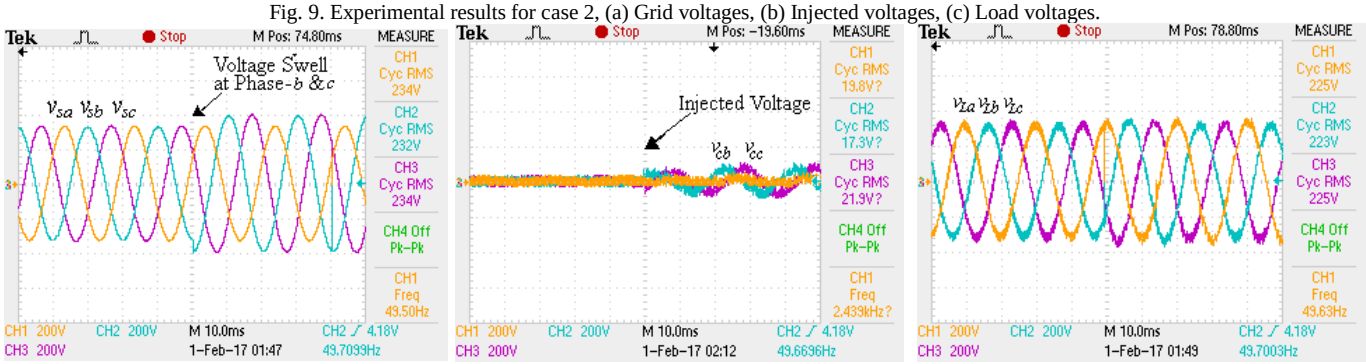


(a) (b) (c)

Fig. 10. Experimental results for case 3, (a) Grid voltages, (b) Injected voltages, (c) Load voltages.

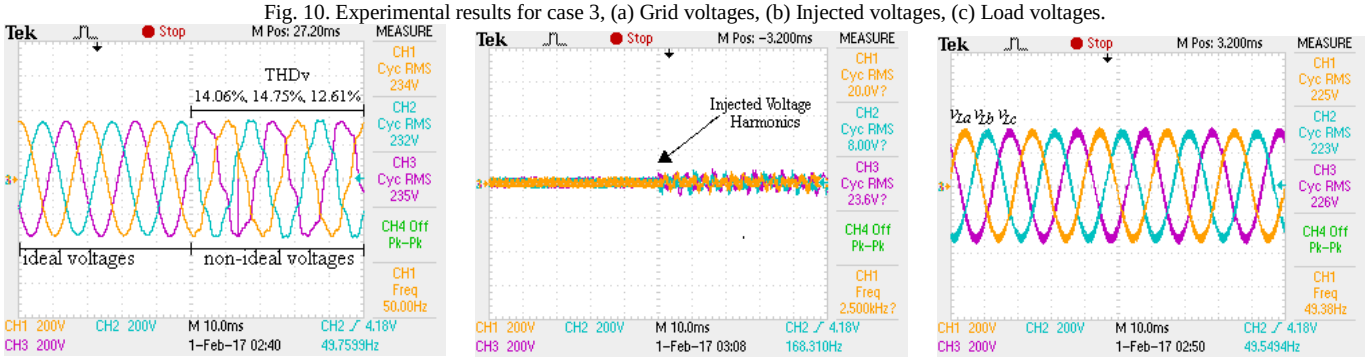


(a) (b) (c)

Fig. 11. Experimental results for case 4, (a) Grid voltages, (b) Injected voltages, (c) Load voltages.

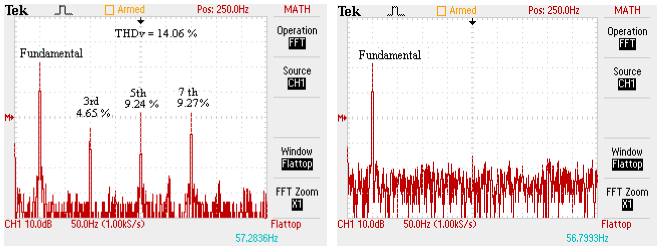


(a) (b)

Fig. 12. Voltage harmonic spectrums for case 4 at phase-A. (a) Grid voltage (b) Load voltage.

## V. Comparisons of the Proposed Method With the State-of-the-Art

It is well known that the occurrence and intensity of voltage-related power quality problems are increasing in grid. This is due to the increase in the number of voltage harmonic-generating devices. In order to overcome these voltage-related power quality problems, several DVR topologies and control methods have been investigated in the literature. A comparison of the proposed method with the state-of-the-art systems in terms of the various features of each method is provided in Table I. The first drawback of the methods presented in [6], [28] and [29] is that they need phase lock loop (PLL) or frequency lock loop (FLL) or low pass filter (LPF) in generating the compensating voltage references which increase the complexity. The proposed controller does not have such problem as ANF generates the compensating voltage references without using PLL, FLL, and LPF. The second drawback of these methods is that they compensate for voltage sags and swells only. In these studies, no result is provided to demonstrate the performance of the controller under distorted grid condition. In contrast, the proposed method not only compensates voltage sags/swells, but also suppresses voltage harmonics on the load terminals and mitigates grid disturbances.

On the other hand, while methods in [28] and [29] require dc-link capacitor to be connected at the input of the inverter, the method in [6] and proposed method require a dc source (battery). The stored energy in the dc-link capacitor may not be sufficient to feed the inverter when the duration of voltage sags/swells is long which degrades the performance of DVR. Although the stored energy in the dc-link capacitor can be increased by selecting a large capacitor, this increases the

cost and, therefore, a compromise between cost and compensation duration should be considered. Furthermore, the computations needed in these control algorithms are high due to the fact that they need abc/dq and dq/abc transformations [6], [28] and fuzzy rule base [6], [29]. Hence, the implementation of the proposed control method is reasonably simpler and computationally efficient than the aforementioned methods. In addition, the methods proposed in [6], [28] and [29] require three, ten and six sensors, respectively, for measuring the voltages and currents needed in the control algorithm. Although the proposed control method requires six voltage sensors, its cost is less than the aforementioned methods when its implementation simplicity and computational requirements are considered. Finally, owing to the inherent feature of SMC, the proposed control method exhibits fast dynamic response which is comparable to that of other methods.

TABLE I: COMPARISONS OF THE PROPOSED CONTROL METHOD WITH OTHER METHODS

| **Comparison Category** | **[6]** | **[28]** | **[29]** | **Proposed Method** |
|---|---|---|---|---|
| Inverter topology | 12-Switch | 12-Switch | 12-Switch | 12-Switch |
| Detection and reference generation | Synchronous reference frame | Synchronous reference frame | Fuzzy logic | Adaptive notch filter |
| Control strategy | Fuzzy logic | Hysteresis voltage control | Proportional-integral control | SMC |
| Ability of sag compensation | Yes | Yes | Yes | Yes |
| Ability of swell compensation | Yes | No | No | Yes |
| Ability of harmonic voltage compensation | No | Yes | No | Yes |
| Ability of unbalanced voltage compensation | Yes | Yes | No | Yes |
| Energy storage | Battery | Capacitor | Capacitor | Battery |
| Dynamic response | Slow | Fast | Fast | Fast |
| Compensation duration | High | Limited | Limited | High |
| Implementation complexity | Complicated | Complicated | Complicated | Simple |
| Cost of the system | Medium | Medium | Medium | Low |

## VI. CONCLUSION

In this study, a SMC strategy is proposed for three-phase DVR using 12-switch VSI. Different from the existing methods, the compensating voltage references required in the SMC are generated by an ANF which shows excellent performance under grid voltage anomalies such as voltage sags, swells, unbalanced and distorted voltage conditions. Unlike existing reference signal generation solutions, the proposed ANF does not require PLL or FLL and low pass filter. Moreover, the use of SMC with its attractive properties makes the control implementation simple. Theoretical considerations are verified by the simulation results as well as the real-time laboratory results over a range of grid voltage anomalies. These results show that the proposed control strategy not only offers an excellent dynamic response independent from the parameter variations and disturbances, but also compensates the voltage sags, swells and harmonics on the load terminals.

## APPENDIX

The system and control parameters of analyzed test system for both simulation and experimental are as follows: $V_{sp} = 230\sqrt{2}\,\mathrm{V}$, $V_{dc} = 600\,\mathrm{V}$, $L = 0.35\,\mathrm{mH}$, $C = 150\mu\,\mathrm{F}$, $\mathrm{Load}_1$=4Ω+10mH, $\mathrm{Load}_2$=24Ω+15mH, $\lambda = 4714$, $\zeta = 0.6$, $\gamma = 18000$. The sampling time is 35μs.

## REFERENCES


[1] M. Ramasamy and S. Thangavel, "Experimental verification of PV based dynamic voltage restorer with significant energy conservation," *Electrical Power and Energy Systems*, vol. 49, pp. 296-307, July 2013.

[2] N. G. Jayanti, M. Basu, I. Axente, K. Gaughan and M. F. Conlon, "Sequence analysis based DSP controller for dynamic voltage restorer (DVR)," In IEEE Power Electronics Specialists Conference (PESC2008), pp. 3986-3991, 15-19 June 2008, Rhodes, Greece.

[3] A. M. Rauf and V. Khadkikar, "An enhanced voltage sag compensation scheme for dynamic voltage restorer," *IEEE Trans. Ind. Electron.*, vol. 62, no. 5, pp. 2683-2692, May 2015.

[4] S. Biricik, S. K. Khadem, S. Redif, and M. Basu, "Control of the dynamic voltage restorer to improve voltage quality," In 5th International Symposium on Power Electronics for Distributed Generation Systems (PEDG 2014), pp. 1-5, Galway, Ireland.

[5] V. D. Mahinda, H. M. Wijekoon and S. S. Choi, "A novel dynamic series compensator with closed-loop voltage and current mode control for voltage sag mitigation," *International Journal of Electronics*, vol. 90, pp. 695-706, 2003.

[6] A. Teke, K. Bayindir, and M. Tumay, "Fast sag/swell detection method for fuzzy logic controlled dynamic voltage restorer," *IET Generation, Transmission & Distribution*, vol. 4, no. 1, pp. 1-12, Jan. 2010.

[7] F. A. L. Jowder, "Design and analysis of dynamic voltage restorer for deep voltage sag and harmonic compensation," *IET Generation, Transmission & Distribution*, vol. 3, no. 6, pp. 547-560, Jun. 2009.

[8] P. Jayaprakash, B. Singh, D. P. Kothari, A. Chandra, and K. Al-Haddad, "Control of reduced-rating dynamic voltage restorer with a battery energy storage system," *IEEE Trans. Ind. Appl.* , vol. 50, no. 2, pp. 1295-1303, March/April 2014.

[9] H. Abdollahzadeh, M. Jazaeri, and A. Tavighi, "A new fast-converged estimation approach for dynamic voltage restorer (DVR) to compensate voltage sags in waveform distortion conditions," *International Journal of Electrical Power & Energy Systems*, vol. 54, pp. 598-609, Jan. 2014.

[10] B. Bae, J. Lee, J. Jeong, and B. Han, "Line-interactive single-phase dynamic voltage restorer with novel sag detection algorithm," *IEEE Trans. Power Delivery*, vol. 25, no. 4, pp. 2702-2709, Oct. 2010.

[11] N. D. Tuyen, G. Fujita, M. N. B. Muhtazaruddin, and T. Funabashi, "Shunt active power filter for 3-phase 3-wire nonlinear load under unbalanced and distorted PCC voltage using notch adaptive filter," In *IEEE PES T&D Conference and Exposition*, pp. 1-5, 2014.

[12] N. D. Dinh, N. D. Tuyen, G. Fujita, and T. Funabashi, "Adaptive notch filter solution under unbalanced and/or distorted point of common coupling voltage for three-phase four-wire shunt active power filter with sinusoidal utility current strategy," *IET Generation, Transmission & Distribution*, vol. 9, no. 13, pp. 1580-1596, 2015.

[13] O. Kukrer, H. Komurcugil, and A. Doganalp, "A three-level hysteresis function approach to the sliding mode control of single-phase UPS inverters," *IEEE Trans. Ind. Electron.*, vol. 56, no. 9, pp. 3477-3486, Sept. 2009.

[14] H. Komurcugil, "Rotating-sliding-line-based sliding-mode control for single-phase UPS inverters," *IEEE Trans. Ind. Electron.*, vol. 59, no. 10, pp. 3719-3726, Oct. 2012.

[15] H. Komurcugil, "Adaptive terminal sliding-mode control strategy for DC-DC buck converters," *ISA Transactions*, vol. 51, no. 6, pp. 673-681, Nov. 2012.
[16] H. Komurcugil, "Non-singular terminal sliding-mode control of DC-DC buck converters," *Control Engineering Practice*, vol. 21, no. 3, pp. 321-332, Mar. 2013.
[17] S. Biricik, H. Komurcugil, and M. Basu, "Sliding mode control strategy-for three-phase DVR employing twelve-switch voltage source converter," in Proc. of 41st Annual Conference of the IEEE Industrial Electronics Society (IECON), 2015 pp. 921-926
[18] H. Komurcugil, and S. Biricik, "Time-Varying and constant switching frequency-based sliding-mode control methods for transformerless DVR employing half-bridge VSI," *IEEE Tran. Ind. Electron.*, vol. 64, no. 4, pp. 2570-2579, 2017.
[19] S. Biricik, H. Komurcugil, "Optimized sliding mode control to maximize existence region for single-phase dynamic voltage restorers," *IEEE Trans. Ind. Inf.*, vol. 12, no.4, pp. 1486-1497, 2016.
[20] Z. Changjiang, V. K. Ramachandaramurthy, A. Arulampalam, C. Fitzer, S. Kromlidis, M. Bames and N. Jenkins, "Dynamic voltage restorer based on voltage-space-vector PWM control," IEEE Trans. Ind. Appl., vol. 37, no. 6, pp. 1855-1863, Nov./Dec. 2001.
[21] C. J Zhan, X. G.Wu, S. Kromlidis V. K. Ramachandaramurthy, M. Barnes, N. Jenkins N, et al. "Two electrical models of the lead-acid battery used in a dynamic voltage restorer," *IEE Proc Gener. Transm. Distrib.*, vol.150, no. 2, pp. 175–182, 2003.
[22] V. K. Ramachandaramurthy, C. Fitzer, A. Arulampalam, C. Zhan, M. Barnes and N. Jenkins, "Control of a battery supported dynamic voltage restorer," *IEE Proc. Gener. Transm. Dist.*, vol. 149, no. 5, pp. 533–542, 2002.
[23] P. Jayaprakash, B. Singh, D. P. Kothari, A. Chandra and K. Al-Haddad, "Control of reduced-rating dynamic voltage restorer with a battery energy storage system," *IEEE Trans. Ind. Appl.*, vol. 50, no. 2, pp. 1295–303, 2014.
[24] E. Babaei, and M. F. Kangarlu, "Comparison four topologies for three-phase dynamic voltage restorer," In Proc. IEEE International Conference on Renewable Energy Research and Applications (ICRERA), 2015, pp. 1527-1532.
[25] M. Mojiri, M. Karimi-Ghartemani and A. Bakhshai, "Time-domain signal analysis using adaptive notch filer," *IEEE Trans. Signal Process.*, vol. 55, no. 1, pp. 85-93, 2007.
[26] D. Yazdani, M. Mojiri, A. Bakhshai, and G. Joos, "A fast and accurate synchronization technique for extraction of symmetrical components," *IEEE Trans. Power Electron.*, vol. 24, no. 3, pp. 674-684, March 2009.
[27] IEEE recommended practices and requirements for harmonic control in electrical power systems, Std. IEEE-519-192.
[28] P. Kanjiya, B. Singh, A. Chandra, and K. Al-Haddad, ""SRF theory revisited" to control self-supported dynamic voltage restorer (DVR) for unbalanced and nonlinear loads," *IEEE Trans. Ind. Appl.*, vo. 49, no. 5, pp. 2330-2340, 2013.
[29] M. Danbumrungtrakul, T. Saengsuwan, and P. Srithorn, "Evaluation of DVR capability enhancement-zero active power tracking technique," *IEEE Access*, vol. 5, pp. 10285-10295, 2017.

**Samet Biricik** (M'12) received the B.Sc. and Ph.D. degrees in electrical and electronic engineering from the Near East University, Nicosia, Mersin 10, Turkey, in 2006 and 2013, respectively. From 2006 to 2016, he worked in various industrial and commercial projects. He is currently a Research Fellow in the School of Electrical and Electronic Engineering of Dublin Institute of Technology, Dublin, Ireland, and a lecturer in the European University of Lefke, Lefke. He is a member of the boards of directors in Chamber of Electrical Engineers in North Cyprus. His research interests include the application of power electronics, power quality, electrical machines, and high-voltage engineering. Dr. Biricik received the Best Paper Award from the IEEE 9th International Conference on Environment and Electrical Engineering in 2010.

**Hasan Komurcugil** (S'94-M'99-SM'12) received the B.Sc., M.Sc. and Ph.D. degrees in electrical engineering from the Eastern Mediterranean University (EMU), Famagusta, North Cyprus, Via Mersin 10, Turkey, in 1989, 1991, and 1998, respectively. In 1998, he joined the Computer Engineering Department, EMU, as an Assistant Professor, where he was promoted to Associate Professor and Professor positions in 2002 and 2008, respectively. From 2004 to 2010, he was the Head of Computer Engineering Department, EMU. In 2010, he played an active role in preparing the department's first self-study report for the use of Accreditation Board for Engineering and Technology. He is currently full-time Professor with the Computer Engineering Department, EMU and Board Member of Higher Education, Planning, Evaluation, Accreditation and Coordination Council (YODAK) North Cyprus. His research interests include power electronics and innovative control methods for power converters. Dr. Komurcugil was the recipient of Best Presentation Recognitions at the 41st and 42nd Annual Conferences of the IEEE Industrial Electronics Society in 2015 and 2016, respectively. He is a corresponding Guest Editor for Emerging Electric Machines and Drives for Smart Energy Conversion in IEEE TRANSACTIONS ON ENERGY CONVERSION. Also, he is an Associate Editor of the IEEE TRANSACTIONS ON INDUSTRIAL ELECTRONICS and IEEE TRANSACTIONS ON INDUSTRIAL INFORMATICS.

**Nguyen Duc Tuyen** received the B.S. degree in electrical engineering from the Hanoi University of Science and Technology, Hanoi, Vietnam, in 2006, and the M.S. and Ph.D. degrees from the Shibaura Institute of Technology, Tokyo, Japan, in 2009 and 2012, respectively. He was a Post-Doctoral Fellow with the Shibaura Institute of Technology, Tokyo, Japan, from 2012 to 2014. From 2014 to 2015, he was a Visiting Researcher with the Shibaura Institute of Technology, Japan. From 2015 to 2017, he was a Project Fellow with the Tokyo University of Science, Japan. From 2017 to 2018, he was the Researcher at National Institute of Advanced Industrial Science and Technology, Japan. Since 2018, he has been with Hanoi University of Science and Technology, Vietnam. His current research interests include distribution power systems, power electronics, renewable energy, smart grids and hydrogen society.

**Malabika Basu** (S'99–M'03) received the B.E. and M.E. degrees in electrical engineering from Bengal Engineering College, Shibpur, Kolkata, India, in 1995 and 1997, respectively, and the Ph.D. degree in electrical engineering from Indian Institute of Technology, Kanpur, Kanpur, India, in 2003. From 2001 to 2003, she was a Lecturer with Jadavpur University, Kolkata, India. From 2003 to 2006, she was a Arnold F. Graves Postdoctoral Fellow with Dublin Institute of Technology, Dublin, Ireland, where she has been a Lecturer from 2006, and a Senior Lecturer since 2016. She has authored or coauthored more than 90 technical publications in various international journals and conference proceedings. Her research interests include grid integration of renewable energy sources, power quality conditioners and power quality control and analysis, photovoltaics and wind energy conversion, and smart grid and microgrids.